Mesospheric Mountain Wave Activity in the Lee of the Southern Andes

P.-D. Pautet[1], M. J. Taylor[1], D. C. Fritts[2], D. Janches[3], N. Kaifler[4], A. Dörnbrack[4], and J. L. Hormaechea[5]

[1]*Center for Atmospheric and Space Sciences/Physics Department, State University, Logan, US*

[2]*GATS, Boulder, US*

[3]*NASA GSFC, Washington, USA*

[4]*Deutsches Zentrum für Luft- und Raumfahrt, Oberpfaffenhaufen, Germany*

[5]*Universidad Nacional de Tierra del Fuego, Rio Grande, Argentina*

Key points:

- A large number of mesospheric mountain wave events are observed in the lee of the Southern Andes under wintertime conditions
- Mountain wave occurrence is highly correlated with the eastward phase of the semi-diurnal tide in the upper mesosphere
- Mountain wave momentum fluxes can reach very large values, revealing their major impact on the upper atmosphere

Abstract

Gravity waves (GWs) generated by orographic forcing, also known as mountain waves (MWs) have been studied for decades. First measured in the troposphere, then in the stratosphere, they were only imaged at mesospheric altitude in 2008. Their characteristics have been investigated during several recent observation campaigns, but many questions remain concerning their impacts on the upper atmosphere, and the effects of the background environment on their deep propagation.

An Advanced Mesospheric Temperature Mapper (AMTM) and the Southern Argentina Agile MEteor Radar (SAAMER) have been operated simultaneously during the Austral winter 2018 from Rio Grande, Argentina (53.8°S). This site is located near the tip of South America, in the lee of the Andes Mountains, a region considered the largest MW hotspot on Earth.

New AMTM image data obtained during a 6-month period show almost 100 occurrences of MW signatures penetrating into the upper mesosphere. They are visible ~30% of time at the height of the winter season (mid-May to mid-July). Their intermittency is highly correlated with the zonal wind controlled by the semi-diurnal tide, revealing the direct effect of the atmospheric background on MW penetration into the Mesosphere Lower Thermosphere (MLT, altitude 80-100 km). Measurements of their momentum fluxes (MF) were determined to reach very large values (average ~250 m^2/s^2), providing strong evidence of the importance and impacts of small-scale gravity waves at mesospheric altitudes.

1. Introduction

Gravity waves (GWs) are major contributors to middle and upper atmosphere dynamics because they account for large momentum and energy transports from sources at lower altitudes, and systematic and variable momentum and energy deposition where they dissipate. Mean

seasonal GW momentum deposition closes the polar mesospheric jets, inducing a pole-to-pole residual circulation, and driving large-scale constituent transport and mean temperatures far from radiative equilibrium (Fritts & Alexander, 2003). GW energy dissipation accompanies breaking and leads to a range of instabilities, turbulence, and local heating and mixing. Their importance has been increasingly recognized over the past six decades, but many GW dynamics and effects have yet to be understood and quantified.

GWs have many sources accompanying weather events in the troposphere and lower stratosphere. Of these, air flow over significant orography that generates mountain waves (MWs) yields the most significant local and statistical responses from the tropopause to the upper stratosphere based on global in-situ and remote-sensing measurements (Eckermann & Preusse, 1999; Fritts & Nastrom, 1992; Hertzog et al., 2012; Jiang et al., 2002).

Tropospheric MWs have been discovered in the 1930s by glider pilots flying over Central Europe (Küttner, 1939a; Küttner, 1939b). Numerous theoretical studies and airborne observations followed, aimed at understanding the vertical propagation of these waves and the hazards they create on air transport (e.g., Scorer, 1949; Eliassen & Palm, 1960; Smith, 1980; Grubišić et al., 2008; Smith, 2019 and references herein). It was only in the 1990s that MWs were measured in the stratosphere using airborne backscatter lidar, radiosonde, balloon, or satellite data (e.g., Eckermann & Preusse, 1999; Dörnbrack et al., 1999, 2002; Wu et al., 2006; Plougonven et al., 2008; Alexander & Teitelbaum, 2011). First mesospheric observations were reported over the El Leoncito Observatory, Argentina, in 2008 (Smith et al., 2009) using airglow image data. Recent satellite measurements over the Southern Andes coupled with raytracing technique, have shown that MWs can even affect the thermosphere (up to ~275 km) through secondary, tertiary or higher-order GW originating from MW breaking (Vadas et al., 2019).

Since, individual instruments have performed more observations, contributing useful, but less comprehensive measurements. Clusters of instruments or dedicated campaigns have enabled much greater and more extensive quantification of MW events and their consequences. Novel imaging, radar and lidar technologies, as well as parallel modeling, are allowing further advances addressing key remaining needs: further investigations can reveal more about the characteristics and variability of major sources and the filtering effects of the background atmosphere.

The characteristics of these MWs at lower altitudes are directly related to the three-dimensional structure of the terrain and the strength of the air flow. However, their responses at higher altitudes depend on the horizontal wind and temperature fields through which they propagate, and with which they often interact strongly (Kruse et al., 2016; Bramberger et al., 2017). Under winter conditions, zonal winds are typically eastward throughout the stratosphere and into the mesosphere from middle to high latitudes, but with magnitudes that vary due to weather systems at lower altitudes and to global planetary waves at higher altitudes.

When zonal winds are eastward and increase strongly in the stratosphere, recent coordinated measurements during the NFS DEEPWAVE campaign (Fritts et al., 2016) have shown that MWs can easily amplify into the mesosphere and attain breaking amplitudes in decreasing winds above (Eckermann et al., 2016; Fritts et al., 2018, 2019; Pautet et al., 2016; Taylor et al., 2019). Weaker or decreasing zonal winds in the stratosphere constrain their amplitudes, but the surviving MWs can nevertheless enable large responses at higher altitudes due to amplitude growth where zonal winds are increasing (Kruse et al., 2016; Bramberger et al., 2017). This is possible because MWs (and generally GWs) undergo breaking at a horizontal perturbation amplitude of $|u_h'| \sim |c - U_h|$, for phase speed c and horizontal mean wind U_h, with a critical level being a special case causing full GW dissipation. Where $|c - U_h|$ remains > 0, breaking does not eliminate the GW, but does generate

92 secondary GWs. The surviving GW grows again with increasing $|c\text{-}U_h|$ and altitude. As a
93 consequence, MW deep penetration into the middle and upper atmosphere can only happen during
94 the winter season, when the zonal wind stays eastward up to the MLT (Scorer, 1949; Schoeberl,
95 1985; Smith et al., 2009).

96 In 2009, Smith et al. showed, using all-sky airglow image data taken in the lee side of the
97 Andes (31.8°S), that MWs can occasionally reach mesospheric altitudes. They observed stationary
98 waves, parallel to the mountain range, several days in a row during the month of July 2008. More
99 recently, several projects including the Deep Propagating Gravity Wave Experiment
100 (DEEPWAVE), and measurements obtained from the Andes Lidar Observatory (ALO, 30.2°S) in
101 Chile, provided more insight on MW propagation into the MLT (Fritts et al., 2016; Hecht et al.,
102 2018). Surprising results including the scale and extent of these MWs (Bossert et al., 2015), or
103 their effects on the upper atmosphere (Eckermann et al., 2016; Pautet et al., 2016; Fritts et al.,
104 2018; Taylor et al., 2019) have been recently published.

105 One of the most interesting results is the intermittent nature of MW occurrence in the
106 mesosphere. Even when the tropospheric forcing persisted several days, MWs were not observed
107 continuously in the MLT during the same period. They appeared and disappeared, as if a gate was
108 opening and closing, blocking their propagation at a lower level or allowing them to penetrate
109 higher up. This result yields the following question: what are the most favorable background
110 atmosphere conditions for MW deep propagation? To answer this question, it is necessary to obtain
111 simultaneous measurements from collocated instruments operating close to a MW hotspot.

112 There are many specific regions on Earth where a variety of MW responses can be observed,
113 but the largest hotspot is located over the southern part of South America during austral winter.
114 Multiple studies have shown that strong tropospheric winds blowing over the Andes generate large

orographic responses in the mesosphere and lower thermosphere (MLT) under suitable propagation conditions (e.g., Eckermann and Preusse, 1999; Jiang et al., 2002; Alexander & Teitelbaum, 2011; Wright et al., 2016). Similar Southern Hemisphere (SH) responses also occur over New Zealand, and are likely over smaller SH islands at higher latitudes, and the coast of Antarctica, given their signatures in the stratosphere (Hendricks et al., 2014), but some of them have yet to be observed in the MLT.

A cluster of novel, high quality instrumentation exists in the lee of the Southern Andes. In Rio Grande, Argentina (53.8°S), a meteor radar (Gats Inc., USA), a Rayleigh lidar (Deutsches Zentrum für Luft- und Raumfahrt, DLR, Germany), an AMTM (Utah state University, USU, USA), and a multi-wavelength all-sky airglow imager (Boston University, BU, USA) have operated jointly since November 2017. During the Austral winter 2018 (mid-March to mid-September) 97 MW signatures were recorded in AMTM image data, allowing for the investigation of the atmospheric conditions conducive to MW deep propagation.

This paper presents these new MW observations, and shows the strong correlation between their occurrence in the mesosphere and the eastward zonal wind, which was found to be mostly controlled by the semi diurnal tide. Section 2 will give an overview of the observation site and the instruments involved in this study. Section 3 will describe the observations, which will be discussed in Section 4. Finally, conclusions will be given in Section 5.

2. Instrumentation

2.1. Estación Astronómica Rio Grande (EARG)

The Rio Grande Observatory (53.8°S, 67.7°W) or Estación Astronómica Rio Grande (EARG) is located in southern Argentina, in the region known as Tierra del Fuego. This site is in close

proximity to a massive knife edge-like mountain chain near-continuously exposed to strong and persistent circumpolar winds, making it part of the most active GW hotspot on Earth (with multiple peaks >1600 m located ~160 km to the WSW, and a more moderate region with peaks <1000 m, ~300 km to the West). The latitude also allows for year-round measurements (no permanent twilight during summer) using autonomous instrument operations.

2.2. Advanced Mesospheric Temperature Mapper

One of the instruments operating at this site, the USU Advanced Mesospheric Temperature Mapper measures the nighttime atmospheric temperature over a ~200x160 km region centered at the zenith, using the OH (3,1) band emission (Pautet et al., 2014). This bright emission originates from a ~7-8 km-thick layer located at ~87 km altitude, and is widely used as a tracer of the dynamical processes in the MLT. The AMTM was designed and built at Utah State University. It uses a 320x256-pixel infrared sensor and a computer-controlled filter wheel to sequentially measure the brightness of the $P_1(2)$ and $P_1(4)$ lines of the OH (3,1) band, as well as the atmospheric background. Combining these three emissions, it is possible to process the OH (3,1) rotational temperature for each pixel of an image and "map" the mesospheric temperature over a large region. Its high spatial (~0.625 km/pix) and temporal (1 temperature map every ~35 s) resolutions, and high precision (1-2 K) allow to measure small and medium-scale GWs characteristics, study GW dissipation and breaking/instabilities, and assess the momentum flux carried by GW events (e.g., Fritts et al., 2014; Bossert et al., 2015; Pautet et al., 2016; 2018; Taylor et al., 2019; Zhao et al., 2019). The AMTM instrument was installed in November 2017 and has operated almost continuously since then.

2.3. SAAMER momentum flux radar

160 The Southern Argentina Agile MEteor Radar (SAAMER) was designed specifically to enable
161 very high-resolution definition of the large-scale wind field and potential sensitivity to GW
162 momentum fluxes employing a generalization of the dual-beam technique (Fritts et al., 2010a). Its
163 frequency and bandwidth are 32.55 and 0.3 MHz, respectively. The transmitter antenna is
164 composed of eight 3-element crossed Yagis arranged in a 27.6 m diameter circle. Its
165 transmit/receive (T/R) switch allows both tropospheric and mesospheric measurements, and the
166 use of the transmitter antennas as a sixth receiver. It is able to measure neutral vertical velocities
167 in the troposphere and MLT. SAAMER has operated at Rio Grande since May 2008. It provides
168 horizontal wind data between ~80-100 km (Fritts et al., 2010b; Wright et al., 2016; de Wit et al.,
169 2016, 2017).
170
171 **3. Observations – Results**
172 **3.1. Mountain wave observations**
173 The OH (3,1) rotational temperature and band intensity were mapped every night during the
174 Austral winter 2018 using the AMTM. In airglow image data, MWs appear as nearly stationary
175 waves that can last several hours, as shown in Figure 1. For easier MW identification, keogram
176 images were automatically generated to summarize each night of observation. These were created
177 by taking the central rows and columns of a series of pictures, and collocating them to produce
178 north-south (NS) and west-east (WE) keogram images, respectively (Taylor et al., 2009). MWs
179 appear as nearly horizontal bands in the WE keogram (because of their near-zero observed zonal
180 phase speed). For example, Figure 2 shows WE keograms in temperature (Figure 2a) and
181 brightness (Figure 2b) for the night of May 21-22, 2018. MW structures are visible until 22:30 UT,
182 and between ~3:00 and ~9:00 UT. Red contours help localize them in the brightness image. After

initial identification in the keograms, each MW occurrence was confirmed by looking at the image data. To be tagged as a MW event, a GW had to last at least 1 hour, with an average horizontal phase speed < 10 m/s for its whole duration.

During the period mid-March to mid-September 2018, which encompasses the Austral winter season, a total of 97 MW events were detected during 78 nights, the earliest being March 30-31, and the latest September 05-06. Such a large number was unexpected but confirms previous, more limited AMTM ground-based observations made from Lauder, New Zealand, as part of the DEEPWAVE campaign. During a 53-night observation period (May 30-31 to July 21-22, 2014) 28 of the 44 clear or partially clear nights showed signs of MWs (64%) (Taylor et al., 2019), providing a first evidence of their potential significant importance at mesospheric altitudes.

To have a better idea of the occurrence frequency of MWs over Rio Grande, their duration was compared to the total hours of clear sky during the nighttime for considered 6-month period. Figure 3 shows the evolution of the MW detection vs the hours of clear sky over the observatory. Viewing conditions were good for 1,314 hours (57.5 % of the 2,285 hours of dark sky observations during these six months), with MWs visible in the AMTM data during 339 hours, corresponding to 25.8 %. This value was highly variable, with most MWs occurring between mid-May and mid-July (~35 %), and more sporadic events detected before and after this period.

MWs observed over Rio Grande exhibit various structures and/or behaviors. Figure 4 shows six examples of the MW patterns recorded during the winter 2018: small-scale waves (λ_x < ~20 km) localized within a wider band (Figure 4a), middle size waves (~20 < λ_x < ~50 km) covering the whole field-of-view (Figure 4b), so-called “sawtooth pattern” (Figure 4c) exhibiting narrow cold regions characteristic of overturning waves, and similar to structures previously observed over New Zealand (Taylor et al., 2019), coincident observations of two different types of structures

(Figure 4d), MW breaking over a large region (4e), and MWs associated with streamwise-aligned instabilities (Figure 4f) (Fritts et al., 2019). Each of these types were observed several times during the 2018 winter season and seemed to correspond to different MW generation and propagation conditions.

The MW parameters (horizontal wavelength λ_h, direction of propagation φ, and temperature perturbation T') were measured using well-developed Fast Fourier Transform (FFT) technique. Results are shown in Figure 5. Because of their nature, MW observed phase speeds are close to zero (e.g., Smith et al., 2009; Smith, 2019), thus not included in the figure. Furthermore, the FFT analysis gives a 180° ambiguity in the direction of propagation, but the eastward tropospheric wind forcing generates westward-propagating MWs and continuous eastward winds at higher altitudes are required to enable MWs to propagate into the mesosphere, thus propagation directions must be between 180° and 360°.

The MW horizontal wavelengths are of the same order (a mean of 25.6 km) as previous airglow non-orographic GW measurements from mid-latitude sites, which ranged between 20 and 30 km for most events (e.g., Hecht et al., 2001 at 40°N; Stockwell and Lowe, 2001 at 42°N; Ejiri et al., 2003 at 35°N and 44°N). The horizontal wavelengths observed in previous MW studies, all of which investigated individual events, varied from 25 km (Bossert et al., 2015), to 36 km (Smith et al., 2009), 40 km (Pautet et al., 2016), 40-71 km (Taylor et al., 2019), and up to ~240 km (Bossert et al., 2015, 2017; Fritts et al., 2018). The larger scales were only observable because the imagers were on a moving platform. The AMTM field-of-view (200 x 160 km) limits the unambiguous detection of MWs to λ_h < 100 km. Larger MWs have a more limited impact on the upper atmosphere, though, with much smaller MF values (Bossert et al., 2015; Fritts et al., 2018).

MW directionality is as expected for this site, with an average direction of propagation equal to 268° (σ = 21°), consistent with an eastward tropospheric wind forcing over the Southern Andes and sustained eastward wind above. There is some variability, though, with values ranging between ~227° and ~318°, which can be explained by irregularities in the direction and amplitude of the forcing, the three-dimensional character of the Southern Andes, and the variability of the atmospheric background between the troposphere and the mesosphere.

The average *T'* is 5.0 K (σ = 3.1 K), with 94% of the amplitudes < 10 K, and a maximum at ~17 K. These are similar to previously published MW *T'* measurements (e.g., Bossert et al., 2015, 4 < *T'* < 8 K, Pautet et al., 2016, *T'* ~ 10 K), but much smaller than the spectacular event described by Taylor et al. (2019), which reached an amplitude of ~37 K.

3.2. Momentum flux calculations

As MWs propagate upward, they transport momentum that resides in the background atmosphere via a pseudo-momentum flux (MF) (Fritts & Alexander, 2003). The MF per unit mass $<u_h'w'>$ for a given wave can be calculated knowing its parameters, as well as the background conditions, using the following equation (Fritts et al., 2014)

$$< u_h'w' >= \frac{g^2 \omega_i}{2N^3} \sqrt{1-\frac{\omega_i^2}{N^2}} \left(\frac{<T'>}{T_0} \right)^2 \frac{1}{C^2} \qquad (1)$$

Here *g* is the acceleration of gravity (9.54 m.s^{-2} at the OH layer), *N* (~0.02 s^{-1}) is the buoyancy frequency, ω_i is the intrinsic frequency, $<T'>$ is the measured temperature perturbation amplitude, T_0 the mean temperature at the altitude of the OH (3,1) emission, and *C* is a factor to compensate for the phase averaging over the finite thickness of the OH layer. It is defined by

$$C = \frac{<T'>}{T'(z_0)} = \exp\left(-3.56 \frac{z_{FWHM}^2}{\lambda_z^2} \right) \qquad (2)$$

where Z_{FWHM} is the full-width half-maximum OH layer thickness (~7 km) and λ_z is the vertical MW wavelength. The triangular parentheses in (1) represent means over both the airglow layer and a complete wave oscillation.

At Rio Grande, the AMTM instrument provided direct measurements of the MW horizontal parameters (wavelength λ_h, direction of propagation φ, temperature perturbation $<T'>$). SAAMER measured the background meridional and zonal wind speed amplitudes u and v, respectively. The vertical wavelength λ_z was then calculated using a simplified version of the dispersion relation, neglecting the wind shear and the wind curvature (smoothly and gradually varying background wind speed, Nappo, 2002)

$$m^2 = \frac{N^2}{(c-U_h)^2} - \frac{1}{4H^2} - k^2 \qquad (3)$$

where N is the buoyancy frequency, c is the observed phase speed (~0 m/s in the case of MWs), U_h is the horizontal wind speed in the direction of the wave, $H = R.T_0/g$ is the scale height (with R = 287 $J.kg^{-1}.K^{-1}$), and $k = 2\pi/\lambda_h$ is the wave horizontal wavenumber. Finally, the vertical wavelength is given by $\lambda_z = 2\pi/m$.

Figure 6 shows the distribution of the MW momentum fluxes over Rio Grande, during the Austral winter 2018. MF values were only obtained for 36 of the 97 identified MW events because the vertical wavelengths in the 61 other cases were indeterminate or very small (<< 10 km) when calculated with (3). Therefore, the cancellation factor C defined in (2) reached very small values, giving unrealistic MF results. Most of those waves were becoming non-linear, as shown by the breaking patterns often simultaneously observed in the image data. Linear theory does not apply in those cases, and therefore equations (1) and (3) have to be used with caution. Nevertheless, the MF values in Figure 6 are consistently large compared to non-orographic GW MF studies (e.g., Tang et al., 2002; Suzuki et al., 2007; Vargas et al., 2009; Cao & Liu, 2016), ranging from ~14 to

~1,000 m^2/s^2, with an average value of 257 m^2/s^2. About half (44%) of the events had a MF < 100 m^2/s^2, but some more sporadic MWs reached values comparable to the largest MFs previously measured (Fritts et al., 2002; Fritts et al., 2014; Taylor et al., 2019).

4. Discussion

4.1. Tropospheric forcing

Mesospheric MWs over Rio Grande are generated in the troposphere when the eastward wind blows over the Southern Andes from the W and SW regions of Tierra del Fuego. Figure 7 shows the zonal wind between 0 and 15 km for March-September 2018, taken from operational analyses and short-term deterministic forecasts of Integrated Forecasting System of the European Center for Medium-Range Weather Forecasts (ECMWF). The model data is retrieved every 6 hours at reduced spectral resolution of wavenumber 21 (approximately 1,000 km horizontal resolution), and interpolated to the location of Rio Grande and to 500 m vertical intervals.

During the period shown in Figure 7, the zonal wind at 2 km (horizontal dashed line) was eastward ~95% of the time, providing almost continuous MW generation the whole winter. When only periods of mesospheric MW observations are taken into account, results are identical (~95%). However, not all the MW sightings correspond exactly to the presence of tropospheric forcing. This suggests that other factors, such as transient forcing or propagation conditions, or MW breaking at lower altitudes may prevent their attainment or clear identification in the MLT. The effects of the background atmosphere on the MW propagation, in particular wind filtering, must play a primary role in the observed MW intermittency.

4.2. Effects of the semi-diurnal tide

As seen for example in Figure 2, MWs were never visible over an entire night, even though the sky was perfectly clear and the tropospheric wind was blowing almost constantly over the mountains. To better understand the penetration of MWs to high altitudes, it is necessary to investigate the horizontal wind variability in the middle and upper atmosphere. Figure 8 shows the zonal wind measured by SAAMER between 80 and 100 km on the night of 21-22 May 2018 (same as Figure 2). The grey shading corresponds to daytime (no AMTM observations), and the blue shading to MWs visible in the airglow image data, which occur in association with periods of eastward wind in the lower part of the figure (~81-84 km). Furthermore, the wind direction appears to alternates from eastward to westward, with a ~12-hr period, indicative of a semi-diurnal tide.

Semi-diurnal tide (SDT) mainly originates from the diurnal heating by solar radiation of the water vapor in the troposphere, and from the ozone in the upper stratosphere and lower mesosphere (Forbes, 1995). Like GWs, it too transports energy and momentum into the MLT, but it also modifies the atmospheric background, affecting the upward propagation of smaller-scale waves. While diurnal tide dominates at low latitudes because of latent heat release in convective processes, the SDT reaches its largest amplitude at mid-latitudes, around 50°, during winter (Hagan et al., 1999; Hagan & Forbes, 2003). Because of this, Rio Grande is an ideal location to study SDT activity. Indeed, using SAAMER data, Fritts et al. (2010a) have shown that SDT is larger than diurnal tide over Southern Argentina, reaching a first maximum in mean monthly amplitude between April and June (with values approaching 80-90 $m.s^{-1}$ above 95 km), and a second maximum between August and October.

Figure 9 summarizes the AMTM and SAAMER observations during the Austral winter 2018. The black line shows MW occurrence in the AMTM data for the period 15 March-15 September, as a percentage of total clear sky time, for each 1-hr bin between 21 UT and 12 UT. The red line

317 is the average SAAMER zonal wind for the same period, between 81 and 84 km altitude. This
318 altitude range corresponds to the bottom part of the OH layer, i.e., the lowest altitude where MWs
319 can be detected by the AMTM. Figure 9 shows high correlation between the airglow MW
320 occurrence and the mesospheric zonal wind variability driven by the SDT, with an almost 12-hr
321 period.

322 Critical level filtering due to winds approaching U_h = 0 m/s plays an important role in GW
323 propagation. If U_h >> 0 m/s, λ_z is large (see Eq. 3), and the GW will freely propagate, transporting
324 momentum to a higher/lower altitude (in the case of an upward/downward-propagating wave). If
325 U_h is approaching 0 m/s (critical level), λ_z will be very small and likely exhibit instabilities that
326 further constrain the amplitude and the airglow response. In the case of MWs, the eastward wind
327 allows MW propagation to higher levels, while westward wind blocks the waves at a lower
328 altitude, acting like a gate to the upper atmosphere.

329 However, eastward wind at 80 km and above does not always yield MW observations. In fact,
330 MWs were recorded in the AMTM data only 29.5% of the time the zonal wind was positive
331 (considering only clear sky conditions), which means that other parameters are important for the
332 MW penetration up to the mesosphere. Recent studies have revealed the effects of several of those
333 parameters. The first one is the horizontal wind minima around 15-25 km, dubbed a “valve layer”,
334 which can attenuate the MWs amplitude and filters part of the wave spectrum, thus allowing MW
335 to propagate to higher altitudes, but with amplitudes attenuated at lower altitudes (Kaifler et al.,
336 2015; Kruse et al., 2016). Another factor can also have a large effect on MW propagation around
337 45-55° latitude: the Polar Night Jet, with strong eastward winds between 40 and 70 km, can
338 partially reflect MWs having sufficiently small λ_hs, or even trap them at the stratopause altitude
339 where $m^2 < 0$ for sufficiently large U_h and/or k_h (see Eq. 3) (Bramberger et al., 2017). Finally,

Taylor et al. (2019) have shown that a 4-hr GW in the MLT modulating the larger-scale wind allowed a spectacular large-amplitude MW to reach the OH layer altitude over the New Zealand South Island on June 21, 2014.

Our observations and discussion reveal that many factors contribute to the complexity of MW propagation into the MLT over a mountainous region in winter conditions. Of the various influences, however, the SDT appears to be the main driver accounting for MW nightly intermittency over Southern Argentina.

4.3. Mountain waves momentum flux

The important role played by GWs in the upper atmosphere can be estimated by assessing their transport of energy and momentum. GW dissipation yields pseudo-momentum deposition that contributes, for example, to the reversal of the mesospheric jets, the residual circulation from the troposphere to the mesosphere, and systematic influences on the large-scale circulation and thermal structures at these altitudes (Fritts & Alexander, 2003).

The MW MFs measured at Rio Grande and presented in Figure 6 correspond to the maximum for each event. In general, these events evolved over the time they were observed in the AMTM data, because of the variability in the forcing, or the horizontal background wind, or the effects of wave breaking which reduces the wave amplitude, therefore decreasing the MF (Fritts et al., 2009; Taylor et al., 2019). In addition, MF estimates are subject to significant measurement uncertainties up to ~35 % or greater (Vargas, 2018). However, the goal of this study is not to provide a detailed, case-by-case analysis of each MW event and its associated MF, but to reveal their intermittency and their anticipated large impacts in the MLT over the Southern Andes. Indeed, Figure 6 shows that the 36 MW events included in this plot had extremely large MFs. The average value (~250 m^2/s^2) was much larger than previous mesospheric GW studies (e.g., Tang et al., 2002; Suzuki et

al., 2007; Vargas et al., 2009). Furthermore, a few rare events had MF >500 m^2/s^2. The importance of these waves has been previously revealed in the stratosphere by balloon measurements obtained over Antarctica. Hertzog et al. (2012) recorded sporadic, very strong events over mountainous regions, such as the Antarctic Peninsula or the Trans-Antarctic Mountain chain. Most importantly, the 1% largest events accounted for ~25% of the total MF during the winter season. Wright et al. (2013) confirmed this result on a near-global scale using satellite data.

The current study shows that, in the MLT as well, such extremely large waves exist over a mountainous region like the Southern Andes where they are generated by orographic forcing. Their MF is much larger than for non-orographic GWs, implying a tremendous impact on the upper atmosphere.

Wright et al. (2013) have also shown that GW intermittency seems to decrease with increasing altitude between 25 and 65 km, attributing this result to the interactions between the waves and the background atmosphere as they propagate away from their sources. Using mesospheric airglow imaging, Cao and Liu (2016) investigated GW MFs and intermittency over two very different locations: Maui, Hawaii (20.8°N, in the Pacific Ocean), and Cerro Pachón, Chile (30.2°S, in the Andes Mountains). Unexpectedly, they found that intermittency was larger over the ocean site, in contrast with stratospheric observations. They explain this result by the possible differences in the propagation conditions between the two sites.

The MW observations over Tierra del Fuego reveal that the GW intermittency is significant over this hotspot, with large, occasional events carrying considerable MF. The intermittency does not depend only on the MW generation, as the tropospheric forcing is almost permanent, but is also highly correlated with the background atmosphere variability, especially the wind filtering in the MLT due to the SDT.

5. Conclusion

Previous satellite measurements have shown that MWs regularly reach the middle and upper stratosphere over the South America-Drake Passage-Antarctic Peninsula hotspot region (e.g., Jiang et al., 2002, 2003, 2005). This paper presents recent multi-instrument observations conducted in the lee of the Southern Andes during the Austral winter 2018. To our knowledge, this is the first extensive investigation of mesospheric MWs covering a complete winter season. The main results are as follows:

- Penetration of MWs as high as the MLT is relatively common. More than 90 events were detected with the USU AMTM imager during a 6-month period, corresponding to ~25% of the clear sky time, with a peak >35% from mid-May to mid-July,
- MW occurrence is highly correlated with the eastward phase of the semi-diurnal tide, which strongly modulates the total eastward wind in the MLT, acting as a gate and modulating the penetration of MF into the upper atmosphere,
- Nevertheless, as the tropospheric forcing is almost permanent in this region, but MWs are not always visible even when the MLT zonal wind is eastward, other processes must also influence MW penetration into the MLT, such as the Polar Night Jet,
- MW MFs are large, with an average of ~250 m^2/s^2 for 36 of the 97 events, providing new evidence of the importance and frequent impacts of MWs on the MLT over this region.

The near permanent orographic forcing in this part of the world makes Southern Argentina an ideal location to study MW life cycles and the various environmental and dynamical influences. The cluster of aeronomy instruments operating in Tierra del Fuego offers an exceptional

opportunity to investigate the complexity of MW deep propagation at this prominent high-latitude site, with extended nighttime airglow observations during the winter season.

Future case-by-case studies involving measurements and model simulations are now needed to help understand the effects of each of the components associated with the complex MW propagation mechanism.

Acknowledgments

The AMTM operated at Rio Grande was designed and built at Utah State University (USU) and the Space Dynamics Laboratory (SDL) with support from the NSF DEEPWAVE grant 1061892. It is currently operated under NSF grant 1651233. The AMTM and ECMWF data used in this study are available through the USU Box (http://digitalcommons.usu.edu/ail/). Password to access the database can be provided upon request to the authors.

DJ's work is supported by the NASA ISFM Heliophysics Program. SAAMER's operation is supported by the NASA SSO Program, NESC assessment TI-17-01204, and NSF grant AGS-1647354. SAAMER data are available on http://cedar.openmadrigal.org

The authors would like to thank the personnel at the Rio Grande Astronomical Observatory (EARG) for their help in installing and operating the AMTM, SAAMER, and CORAL instruments, in particular the invaluable support of Carlos Ferrer, Gerardo Connon, and Luis Barbero.

References

Alexander, M. J., & H. Teitelbaum (2011). Three-dimensional properties of Andes mountain waves observed by satellite: A case study, *Journal of Geophysical Research*, **116**, D23110, doi:10.1029/2011JD016151.

Bossert, K., D. C. Fritts, P.-D. Pautet, B. P. Williams, M. J. Taylor, B. Kaifler, A. Dornbrack, I. M. Reid, D. J. Murphy, A. J. Spargo, and A. D. MacKinnon (2015). Momentum flux estimates accompanying multi-scale gravity waves over Mt. Cook, New Zealand on 13 July 2014 during the DEEPWAVE campaign, *Journal of Geophysical Research*, **120**, 9323–9337, doi: 10.1002/2015JD023197.

Bossert, K., C. G. Kruse, C. J. Heale, D. C. Fritts, B. P. Williams, J. B. Snively, P.-D. Pautet, and M. J. Taylor (2017). Secondary gravity wave generation over New Zealand during the DEEPWAVE campaign, *Journal of Geophysical Research: Atmosphere*, **122**, 7834–7850, doi:10.1002/2016JD026079.

Bramberger, M., A. Dörnbrack, K. Bossert, B. Ehard, B. Kaifler, C. Mallaun, A. Orr, P.-D. Pautet, M. Rapp, M. J. Taylor, S. Vosper, B. P. Williams, and B. Witschas (2017). Does strong tropospheric forcing cause large-amplitude mesospheric gravity waves? A DEEPWAVE case study, *Journal of Geophysical Research: Atmosphere*, **122**, doi.org/10.1002/2017JD027371.

Cao, B., & A. Z. Liu (2016). Intermittency of gravity wave momentum flux in the mesopause region observed with an all-sky airglow imager, *Journal of Geophysical Research: Atmosphere*, **121**, doi:10.1002/2015JD023802.

de Wit, R. J., D. Janches, D. C. Fritts, and R. E. Hibbins (2016). QBO modulation of the mesopause gravity wave momentum flux over Tierra del Fuego, *Geophysical Research Letters*, **43**, 4049–4055, doi:10.1002/2016GL068599.

de Wit, R. J., D. Janches, D. C. Fritts, R. G. Stockwell, and L. Coy (2017). Unexpected climatological behavior of MLT gravity wave momentum flux in the lee of the Southern Andes hot spot, *Geophysical Research Letters*, **44**, 1182–1191, doi:10.1002/2016GL072311.

Dörnbrack, A., Leutbecher, M., Kivi, R. and Kyrö, E. (1999). Mountain wave induced record low stratospheric temperatures above Northern Scandinavia, *Tellus*, **51A**, 951-963.

Dörnbrack, A., T. Birner, A. Fix, H. Flentje, A. Meister, H. Schmid, E. V. Browell, and M. J. Mahoney (2002). Evidence for inertia gravity waves forming polar stratospheric clouds over Scandinavia, *Journal of Geophysical Research*, **107**(D20), 8287, doi:10.1029/2001 JD000452.

Eckermann, S. D., and P. Preusse (1999). Global measurements of stratospheric mountain waves from space, *Science*, **286**, 1534– 1537.

Eckermann, S. D., Broutman D., Ma J., Doyle J. D., Pautet P.-D., Taylor M. J., Bossert K., Williams B. P., Fritts D. C., and Smith R. B. (2016). Dynamics of orographic gravity waves observed in the mesosphere over Auckland Islands during the Deep Propagating Gravity Wave Experiment (DEEPWAVE), *Journal of Atmospheric Sciences*, doi: 10.1175/JAS-D-16-0059.1

Eliassen, A., & E. Palm (1960). On the transfer of energy in stationary mountain waves. *Geofysiske Publikasjoner*, **22**, 1–23.

Ejiri, M. K., K. Shiokawa, T. Ogawa, K. Igarashi, T. Nakamura, and T. Tsuda (2003). Statistical study of short-period gravity waves in OH and OI nightglow images at two separated sites, *Journal of Geophysical Research*, **108** (D21), 4679, doi:10.1029/2002JD002795.

Forbes, J. M. (1995). Tidal and planetary waves, in The Upper Mesosphere and Lower Thermosphere: A Review of Experiment and Theory, *Geophysics Monography Series*, **87**, edited by R. M. Johnson and T. L. Killeen, pp. 67– 87, AGU, Washington, D. C.

476 Fritts, D. C., and G. D. Nastrom (1992), Sources of mesoscale variability of gravity waves. Part
477 II. Frontal, convective, and jet stream excitation, *Journal of Atmospheric Sciences*, **49**, 111–
478 127.
479 Fritts, D. C., S. L. Vadas, and Y. Yamada (2002). An estimate of strong local body forcing and
480 gravity wave radiation based on OH airglow and meteor radar observations, *Geophysical*
481 *Research Letters*, **29**, 10, 1429, doi:10.1029/2001GL013753.
482 Fritts, D. C., & M. J. Alexander (2003). Gravity wave dynamics and effects in the middle
483 atmosphere, *Review of Geophysics*, **41**, 1003, doi:10.1029/2001RG000106.
484 Fritts, D. C., Wang, L., Werne, J., Lund, T., & Wan, K. (2009). Gravity wave instability dynamics
485 at high Reynolds numbers, 1: Wave field evolution at large amplitudes and high frequencies,
486 *Journal of the Atmospheric Sciences*, **66**, 1126–1148, doi.org/10.1175/2008JAS2726.1.
487 Fritts, D.C., D. Janches, H. Iimura, W. K. Hocking, N. J. Mitchell, B. Fuller, B. Vandepeer, J.
488 Hormaechea, C. Brunini, and H. Levato (2010a). Southern Argentina Agile Meteor Radar
489 (SAAMER): System design and initial measurements of large-scale winds and tides, *Journal*
490 *of Geophysical Research*, doi:10.1029/2010JD013850.
491 Fritts, D. C., D. Janches, and W. K. Hocking (2010b). Southern Argentina Agile Meteor Radar:
492 Initial assessment of gravity wave momentum fluxes, *Journal of Geophysical Research*, **115**,
493 D19123, doi:10.1029/2010JD013891.
494 Fritts, D. C., P.-D. Pautet, K. Bossert, M. J. Taylor, B. P. Williams, H. Iimura, T. Yuan, N. J.
495 Mitchell, and G. Stober (2014). Quantifying Gravity Wave Momentum Fluxes with
496 Mesosphere Temperature Mappers and Correlative Instrumentation, *Journal of Geophysical*
497 *Research*, doi: 10.1002/2014JD022150.

Fritts, D. C., Smith R. B., Taylor M. J., Doyle J. M., Eckermann S. E., Dörnbrack A., Rapp M., Williams B. P., Pautet P.-D., Bossert K., Criddle N. R., Reynolds C. A., Reineke A., Uddstrom M., Revell M. J., Turner R., Kaifler B., Wagner J. S., Mixa T., Kruse C. G., Nugent A. D., Watson C. D., Gisinger S., Smith S. M., Moore J. J., Brown W. O., Haggerty J. A, Rockwell A., Stossmeister G. J., Williams S. F., Hernandez G., Murphy D. J., Klekociuk A., Reid I. M., and Ma J. (2016). The Deep Propagating Gravity Wave Experiment (DEEPWAVE): An airborne and ground-based exploration of gravity wave propagation and effects from their sources throughout the lower and middle atmosphere, *Bulletin of the American Meteorological Society*, doi: 10.1175/BAMS-D-14-00269.1.

Fritts, D. C., Vosper, S. B., Williams, B. P., Bossert, K., Plane, J. M. C., Taylor, M. J., et al. (2018). Large-amplitude mountain waves in the mesosphere accompanying weak cross-mountain flow during DEEPWAVE Research Flight RF22, *Journal of Geophysical Research: Atmospheres*, **123**, doi.org/10.1029/2017JD028250.

Fritts, D. C., Wang, L., Taylor, M. J., Pautet, P.-D., Criddle, N. R., Kaifler, B., et al. (2019). Large-amplitude mountain waves in the mesosphere observed on 21 June 2014 during DEEPWAVE: 2. Nonlinear dynamics, wave breaking, and instabilities, *Journal of Geophysical Research: Atmospheres*, **124**. https://doi.org/10.1029/2019JD030899.

Grubišić, V., J. D. Doyle, J. Kuettner, S. Mobbs, R. B. Smith, C. D. Whiteman, R. Dirks, S. Czyzyk, S. A. Cohn, S. Vosper, M. Weissmann, S. Haimov, S. F. J. De Wekker, L. L. Pan, and F. Katopodes Chow (2008). The Terrain-Induced Rotor Experiment: A field campaign overview including observational highlights, *Bulletin of the American Meteorological Society*, **89**, 1513–1533, doi.org/10.1175/2008BAMS2487.1.

Hagan, M. E., M. D. Burrage, J. M. Forbes, J. Hackney, W. J. Randel, and X. Zhang (1999). GSWM-98: Results for migrating solar tides, *Journal of Geophysical Research*, **104**(A4): 6813–6827.

Hagan, M. E., & J. M. Forbes (2003). Migrating and non-migrating semidiurnal tides in the upper atmosphere excited by tropospheric latent heat release, *Journal of Geophysical Research*, **108**(A2), 1062, doi:10.1029/2002JA009466.

Hecht, J. H., R. L. Walterscheid, M. Hickey, and S. Franke (2001). Climatology and modeling of quasi-monochromatic atmospheric gravity waves observed over Urbana, Illinois, *Journal of Geophysical Research*, **106** (D6), 5181–5196.

Hecht, J. H., Fritts, D. C., Wang, L., Gelinas, L. J., Rudy, R. J., Walterscheid, R. L., Franke, S. J. (2018). Observations of the breakdown of mountain waves over the Andes Lidar Observatory at Cerro Pachon on 8/9 July 2012. *Journal of Geophysical Research: Atmospheres*, **123**, 276–299, doi.org/10.1002/2017JD027303.

Hendricks, E., J. M. Doyle, S. D. Eckermann, Q. Jiang, and P. A. Reinecke (2014), What is the source of the stratospheric gravity wave belt in austral winter?, *Journal of Atmospheric Sciences*, **71**, 1583–1592, doi:10.1175/JAS-D-13-0332.1.

Hertzog, A., M. J. Alexander, and R. Plougonven (2012). On the intermittency of gravity wave momentum flux in the stratosphere, *Journal of Atmospheric Sciences*, **69**(11), 3433–3448.

Jiang, J. H., D. L. Wu, and S. D. Eckermann (2002). Upper Atmosphere Research Satellite (UARS) MLS observation of mountain waves over the Andes, *Journal of Geophysical Research*, **107**, D22, 10.1029 /2002JD002091.

541 Jiang, J. H., D. L. Wu, S. D. Eckermann, and J. Ma (2003). Mountain waves in the middle
542 atmosphere: microwave limb sounder observations and analyses, *Advances in Space Research,*
543 **32**, 801–806.
544 Jiang, J. H., S. D. Eckermann, D. L. Wu, K. Hocke, B. Wang, J. Ma, and Y. Zhang (2005). Seasonal
545 variation of gravity wave sources from satellite observation, *Advances in Space Research*,
546 doi:10.1016/j.asr.2005.01.099.
547 Kaifler, B., N. Kaifler, B. Ehard, A. Dörnbrack, M. Rapp, and D. C. Fritts (2015). Influences of
548 source conditions on mountain wave penetration into the stratosphere and
549 mesosphere, *Geophysical Research Letters,* doi: 10.1002/2015GL066465. ISSN 0094-8276.
550 Kruse, C. G., R. B. Smith, and S. D. Eckermann (2016). The midlatitude lower-stratospheric
551 mountain wave "valve layer", *Journal of Atmospheric Sciences*, **73**(12), 5081–5100,
552 doi.org/10.1175/JAS-D-16-0173.1.
553 Küttner, J. (1939a). Moazagotl und Föhnwelle, *Beiträge zur Physik der freien Atmosphäre*, **25**, 79-
554 114.
555 Küttner, J (1939b). Zur Entstehung der Föhnwelle, *Beiträge zur Physik der freien Atmosphäre*, **25**,
556 251-299.
557 Nappo, C. J. (2002). Atmospheric Gravity Waves, *International Geophysical Series*, **85**,
558 Academic, San Diego, Calif.
559 Pautet, P.-D., Taylor M. J., Pendleton W. R. Jr, Zhao Y., Yuan T., Esplin R., and McLain D.
560 (2014). An Advanced Mesospheric Temperature Mapper for high-latitude airglow studies,
561 *Applied Optics*, **53** (26), 5934-5943.
562 Pautet, P.-D., Taylor M. J., Fritts D. C., Bossert K., Williams B. P., Broutman D., Ma J.,
563 Eckermann S. D., and Doyle J. (2016). Large amplitude mesospheric response to an orographic

564 wave generated over the Southern Ocean Auckland Islands (50.7°S) during the DEEPWAVE
565 project, *Journal of Geophysical Research*, 10.1002/2015JD024336.
566 Pautet, P.-D., M. J. Taylor, J. B. Snively, and C. Solorio (2018). Unexpected occurrence of
567 mesospheric frontal gravity wave events over South Pole (90°S), *Journal of Geophysical*
568 *Research: Atmosphere*, **123**, doi.org/10.1002/2017JD027046.
569 Plougonven, R., A. Hertzog, and H. Teitelbaum (2008). Observations and simulations of a large-
570 amplitude mountain wave breaking over the Antarctic Peninsula, *Journal of Geophysical*
571 *Research*, **113**, doi:10.1029/2007JD009739.
572 Schoeberl, M. R. (1985). The penetration breakdown of mountain waves into the middle
573 atmosphere, *Journal of Atmospheric Science*, **42**, 2856– 2864.
574 Scorer, R. S. (1949). Theory of waves in the lee of mountains, *Quarterly Journal of Royal*
575 *Meteorology Society*, **75**, 41– 56.
576 Smith, R. B. (1980). Linear theory of stratified hydrostatic flow past an isolated mountain, *Tellus*,
577 **32**, 348–364, doi:10.1111/j.2153-3490.1980.tb00962.x.
578 Smith, R. B. (2019). 100 years of progress on mountain meteorology research, *American*
579 *Meteorological Society*, https://doi.org/10.1175/AMSMONOGRAPHS-D-18-0022.1.
580 Smith, S. M., J. Baumgardner, and M. Mendillo (2009). Evidence of mesospheric gravity-waves
581 generated by orographic forcing in the troposphere, *Geophysical Research Letters*, **36**, L08807,
582 doi:10.1029/2008GL036936.
583 Stockwell, R. G., & R. P. Lowe (2001). Airglow imaging of gravity waves: 1. Results from a small
584 network of OH nightglow scanning imagers, *Journal of Geophysical Research*, **106** (D15),
585 17,185–17,203.

586 Suzuki, S., K. Shiokawa, Y. Otsuka, T. Ogawa, M. Kubota, M. Tsutsumi, T. Nakamura, and D. C.
587 Fritts (2007). Gravity wave momentum flux in the upper mesosphere derived from OH airglow
588 imaging measurements, *Earth Planets Space*, **59**, 421–428.
589 Tang, J., A. Z. Liu, and G. R. Swenson (2002). High frequency gravity waves observed in OH
590 airglow at Starfire Optical Range, NM: Seasonal variations in momentum flux, *Geophysical*
591 *Research Letters*, **29**, 20, 1966, doi:10.1029/2002GL015794.
592 Taylor, M. J., Pautet P.-D., Medeiros A. F., Buriti R. A., Fechine J., Fritts D. C., Vadas S. L.,
593 Takahashi H., and São Sabbas F. T. (2009). Characteristics of mesospheric gravity waves near
594 the magnetic equator, Brazil during the SpreadFEx campaign, *Annales Geophysicae*, **27**, 461–
595 472.
596 Taylor, M. J., P.-D. Pautet, D. C. Fritts, B. Kaifler, S. M. Smith, Y. Zhao, N. R. Criddle, P.
597 McLaughlin, W. R. Pendleton, Jr., M. McCarthy, G. Hernandez*, S. D. Eckermann, J. Doyle,
598 M. Rapp, B. Liley, and J. M. Russell III (2019). Large-Amplitude Mountain Waves in the
599 Mesosphere Observed on 21 June 2014 During DEEPWAVE: 1. Wave Development, Scales,
600 Momentum Fluxes, and Environmental Sensitivity, *Journal of Geophysical Research:*
601 *Atmosphere*, **124**, doi.org/ 10.1029/2019JD030932.
602 Vadas, S. L., Xu, S., Yue, J., Bossert, K., Becker, E., and Baumgarten, G. (2019). Characteristics
603 of the quiet-time hotspot gravity waves observed by GOCE over the Southern Andes on 5 July
604 2010. *Journal of Geophysical Research: Space Physics*, **124**. doi.org/10.1029/2019JA026693
605 Vargas, F., D. Gobbi, H. Takahashi, and L. M. Lima (2009). Gravity wave amplitudes and
606 momentum fluxes inferred from OH airglow intensities and meteor radar winds during
607 SpreadFEx, *Annales Geophysicae*, **27**, 1–9.

Vargas, F. (2018). Uncertainties in gravity wave parameters, momentum fluxes, and flux divergences estimated from multi-layer measurements of mesospheric nightglow layers, *Advances in Space Research*, doi:10.1016/j.asr.2018.09.039.

Wright, C. J., S. M. Osprey, and J. C. Gille (2013). Global observations of gravity wave intermittency and its impact on the observed momentum flux morphology, *Journal of Geophysical Research: Atmosphere*, **118**, 10,980–10,993, doi:10.1002/jgrd.50869.

Wright, C. J., Hindley, N. P., Moss, A. C., and Mitchell, N. J. (2016). Multi-instrument gravity-wave measurements over Tierra del Fuego and the Drake Passage – Part 1: Potential energies and vertical wavelengths from AIRS, COSMIC, HIRDLS, MLS-Aura, SAAMER, SABER and radiosondes, *Atmospheric Measurement Techniques*, **9**, 877-908, doi:10.5194/amt-9-877-2016.

Wu, D. L., P. Preusse, S. D. Eckermann, J. H. Jiang, M. de la Torre Juarez, L. Coy, and D. Y. Wang (2006). Remote sounding of atmospheric gravity waves with satellite limb and nadir techniques, *Advances in Space Research*, **37**, 2269–2277.

Zhao, Y., Taylor, M. J., Pautet, P.-D., Moffat-Griffin, T., Hervig, M. E., Murphy, D. J., et al. (2019). Investigating an unusually large 28-day oscillation in mesospheric temperature over Antarctica using ground-based and satellite measurements, *Journal of Geophysical Research: Atmospheres*, **124**, 8576–8593, doi.org/10.1029/2019JD030286.

Figure captions:

Figure 1: Series of OH (3,1) temperature maps (at ~12 min intervals) showing the quasi stationary signature of a mesospheric mountain wave event which occurred on the night of June 02-03, 2018. The black region at the bottom of the images is due to the projection technique, and the black spot moving westward is the full moon.

Figure 2: Keogram images summarizing the observations for the night of May 21-22, 2018. Top: OH rotation temperature, Bottom: OH brightness. Mountain waves appear as horizontal bands between 22:30 UT and between 3:00 and 9:00 UT. They are emphasized with red loops on the brightness keogram (bottom).

Figure 3: Mountain wave occurrence vs hours of clear sky between March 15th and September 15th, 2018.

Figure 4: Series of AMTM brightness images illustrating the different types of structures and behaviors exhibited by MWs during the winter 2018. (a) localized short-scale waves, (b) extensive pattern covering the whole field-of-view, (c) sawtooth pattern, (d) coincident structure (a) and (c), (e) MW breaking, (f) streamwise vortices.

Figure 5: MW parameters distributions. (a) Horizontal wavelength, (b) temperature perturbation amplitude, and (c) direction of propagation.

Figure 6: MF distribution for 36 MW events.

Figure 7: ECMWF tropospheric zonal wind between March and September 2018.

Figure 8: SAAMER zonal wind data for May 21-22, 2018. The grey shading corresponds to daytime (no AMTM data), and the blue shading to MW observations.

Figure 9: Correlation between nightly average MW occurrence and average zonal wind at 81-84 km, for the Austral winter 2018.

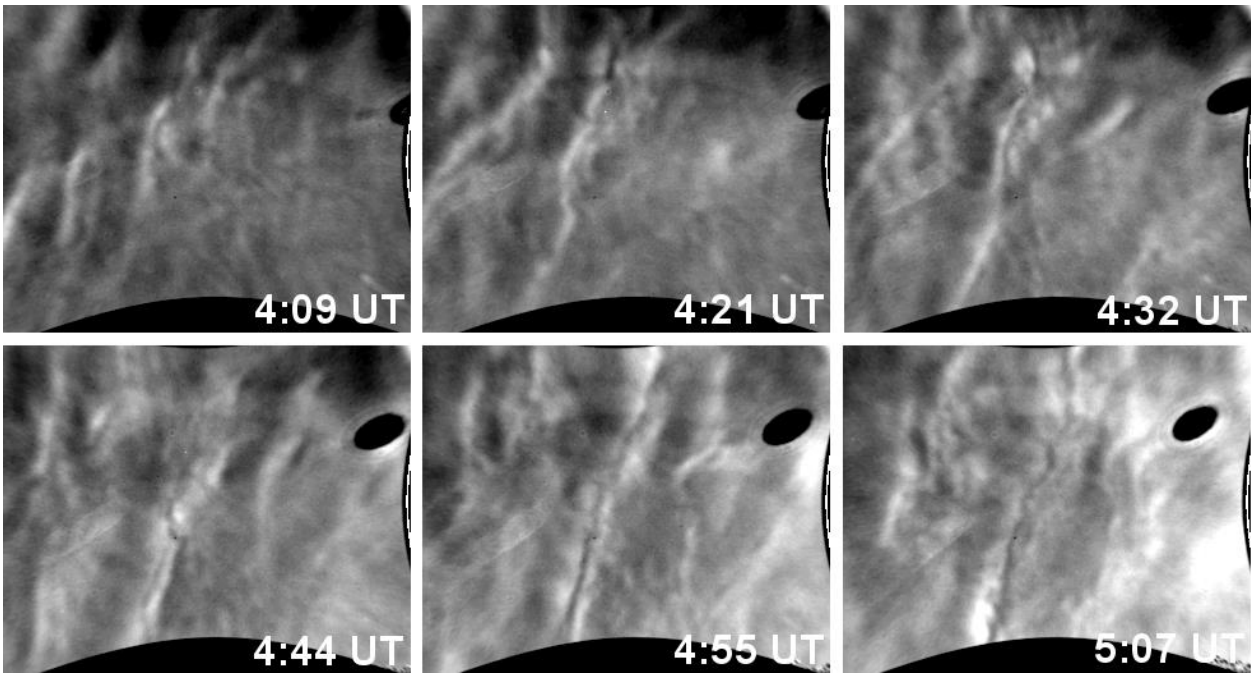

Figure 1.

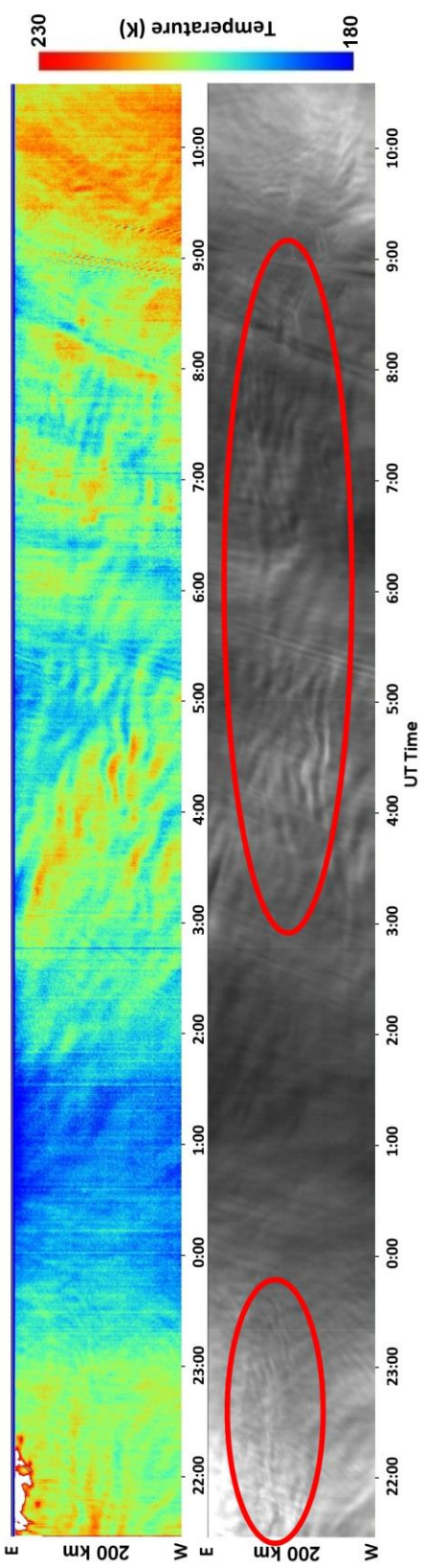
230
Temperature (K)
180
E
200 km
W
E
200 km
W
10:00
9:00
8:00
7:00
6:00
5:00
4:00
3:00
2:00
1:00
0:00
23:00
22:00
UT Time

Figure 2.

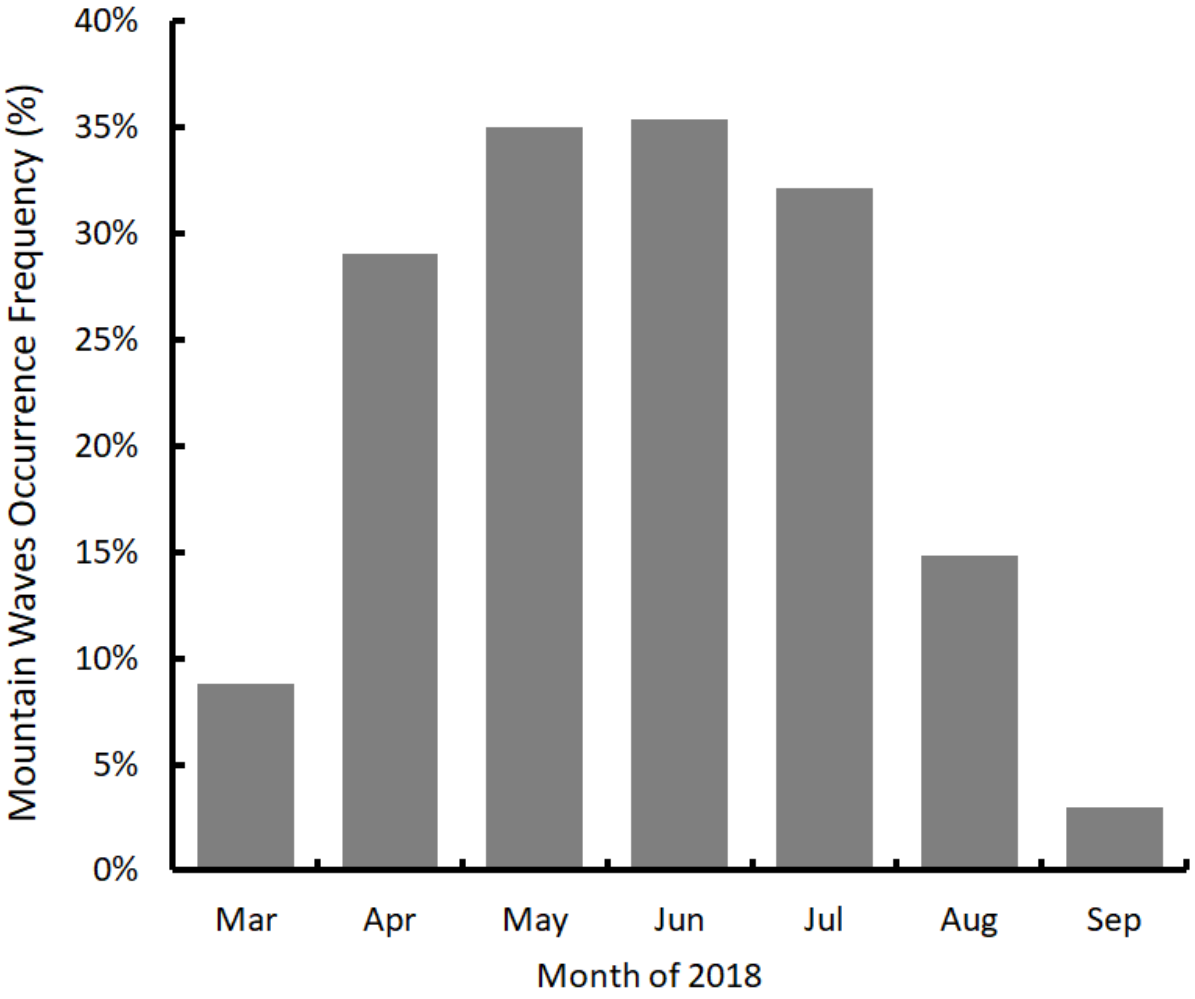
Mountain Waves Occurrence Frequency (%)
40%
35%
30%
25%
20%
15%
10%
5%
0%
Mar
Apr
May
Jun
Jul
Aug
Sep
Month of 2018

Figure 3.

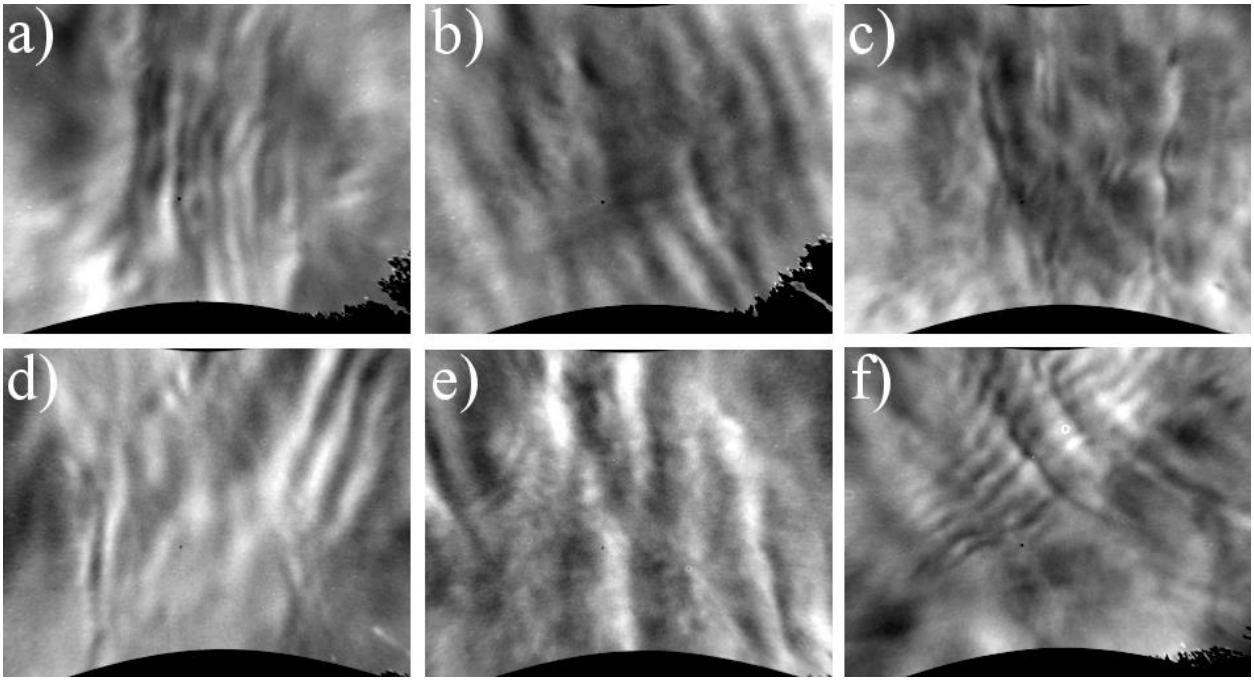

Figure 4.

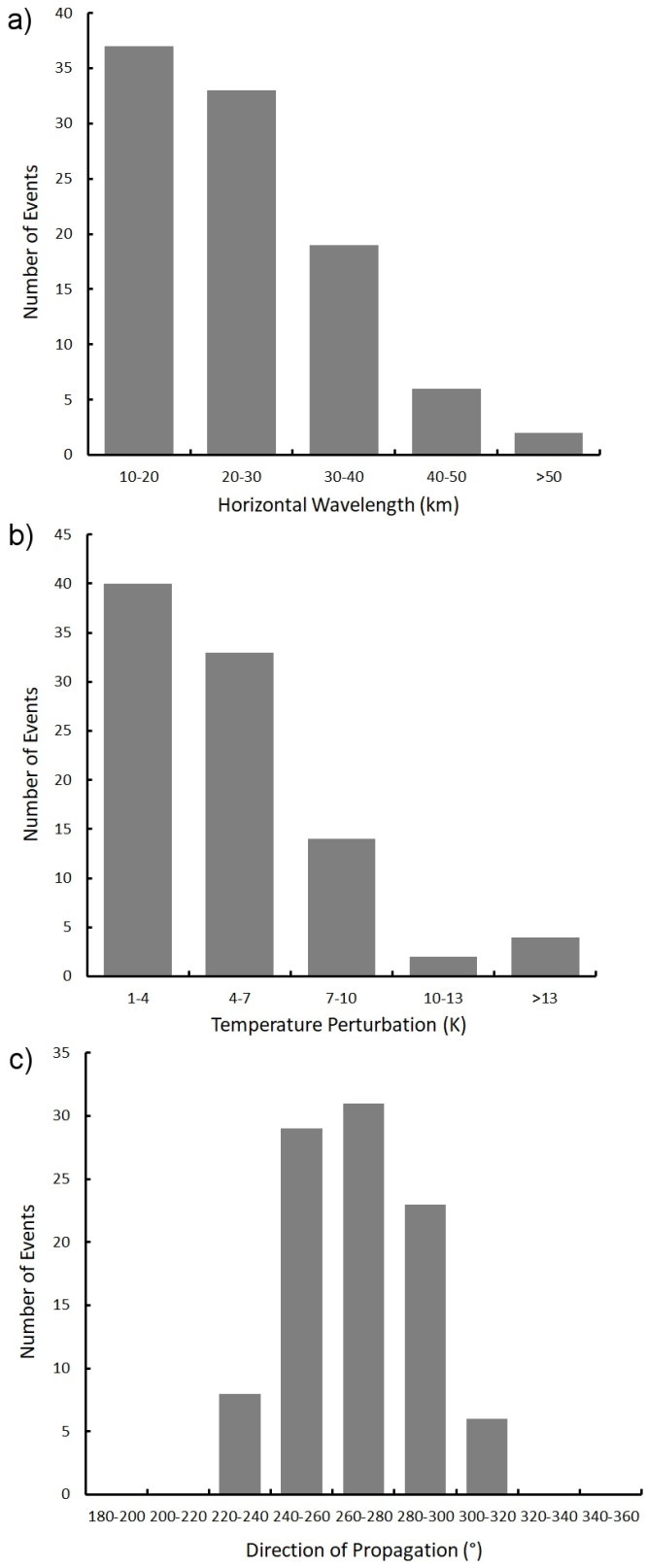
a)
Number of Events
0
5
10
15
20
25
30
35
40
10-20
20-30
30-40
40-50
>50
Horizontal Wavelength (km)
b)
Number of Events
0
5
10
15
20
25
30
35
40
45
1-4
4-7
7-10
10-13
>13
Temperature Perturbation (K)
c)
Number of Events
0
5
10
15
20
25
30
35
180-200
200-220
220-240
240-260
260-280
280-300
300-320
320-340
340-360
Direction of Propagation (°)

Figure 5.

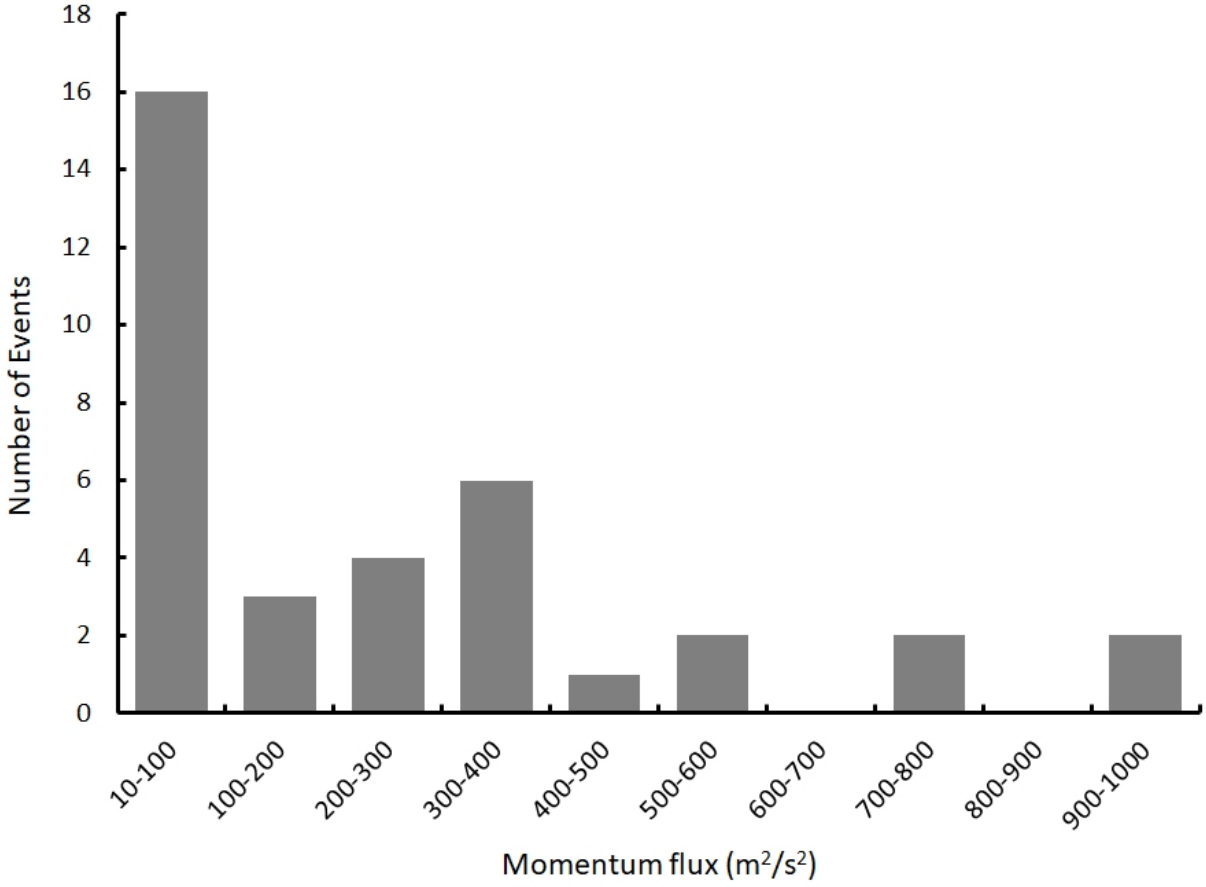
18
16
14
12
10
8
6
4
2
0
Number of Events
10-100
100-200
200-300
300-400
400-500
500-600
600-700
700-800
800-900
900-1000
Momentum flux (m²/s²)

Figure 6.

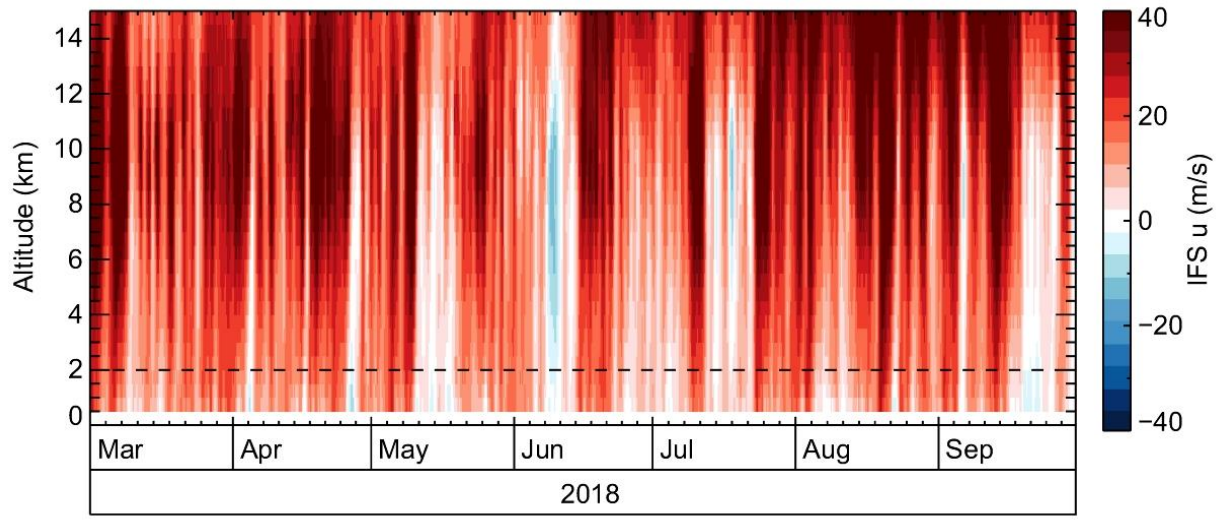
Altitude (km)
0
2
4
6
8
10
12
14
Mar
Apr
May
Jun
Jul
Aug
Sep
2018
40
20
0
−20
−40
IFS u (m/s)

Figure 7.

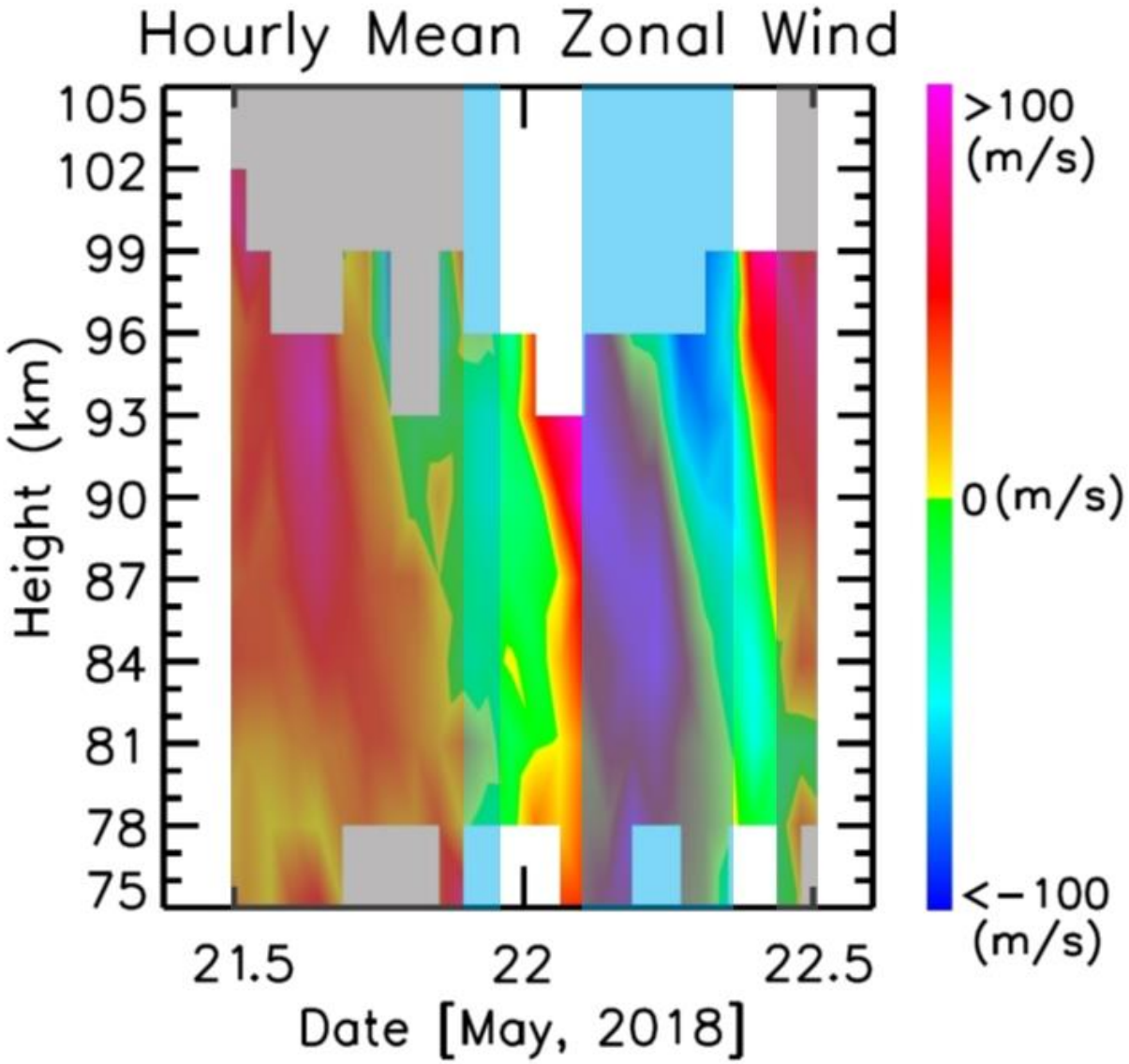
Hourly Mean Zonal Wind
105
102
99
96
93
90
87
84
81
78
75
Height (km)
21.5
22
22.5
Date [May, 2018]
>100
(m/s)
0 (m/s)
<−100
(m/s)

Figure 8.

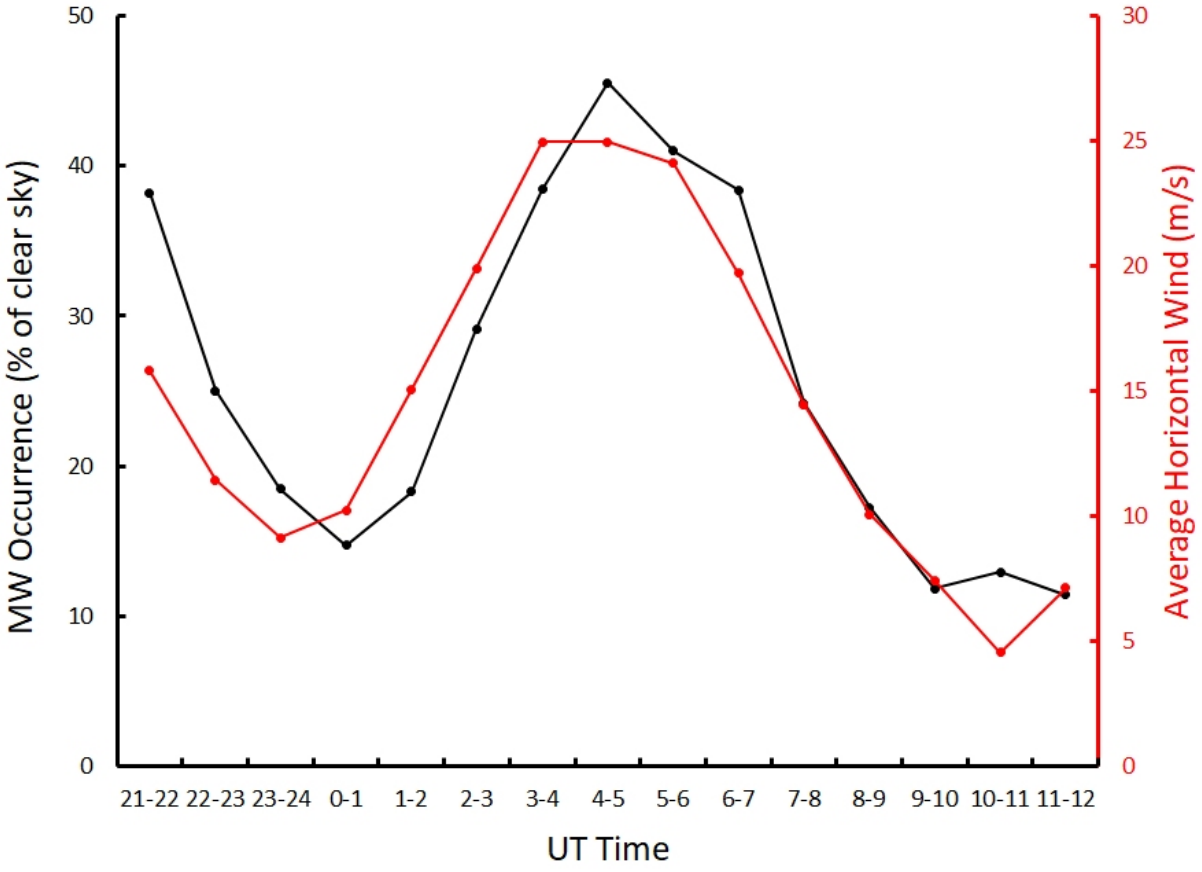
MW Occurrence (% of clear sky)
Average Horizontal Wind (m/s)
UT Time
0
10
20
30
40
50
0
5
10
15
20
25
30
21-22
22-23
23-24
0-1
1-2
2-3
3-4
4-5
5-6
6-7
7-8
8-9
9-10
10-11
11-12

Figure 9.